Growth and atomic structure of ordered Mn surface alloys on Au(001)

Wondong Kim* and S.-J. Oh
Department of Physics and Center for Strongly Correlated Materials, Seoul National University, Seoul 151-742, Korea

Jikeun Seo
Division of General Education, Chodang University, Muan 524-800, Korea

H. G. Min
Department of Physics, Hong-Ik University, Seoul 121-791, Korea

S. C. Hong
Department of Physics, University of Ulsan, Ulsan 680-749, Korea

J.-S. Kim
Department of Physics, Sook-Myung Women's University, Seoul 140-742, Korea
(Received 2 July 2001; revised manuscript received 8 January 2002; published 13 May 2002)

The atomic structures of two different, ordered Mn surface alloys on Au(001) are studied by the low-energy electron diffraction *IV* (spot intensity vs incident electron energy) analysis. The first one is formed of a subsurface $c(2\times2)$ alloy layer beneath 1-monolayer- (ML) thick Au capping layer, 1-ML Au/1-ML $c(2\times2)$ Au-Mn/Au(001). The atomic structure is just like the bulk terminated $Au_3Mn(001)$ with small surface relaxation. The second alloy film is largely formed of trilayer, $AuMn_3(001)$-like structure, $c(2\times2)$ 1-ML Au-Mn/1-ML Mn/1-ML $c(2\times2)$Mn-Au/Au(001), where the position of Mn and Au in the third layer is exchanged with respect to those of the first layer to reduce the strain normal to the surface. Contrary to the first-ordered alloy, we find large contraction of the layer spacing and the strong buckling of Mn atoms in the surface layer for the second one. We discuss the energetics relevant to the formation of the observed alloy structures.

DOI: 10.1103/PhysRevB.65.205407 PACS number(s): 68.35.−p, 68.37.−d

I. INTRODUCTION

For the last decades, ultrathin magnetic films on nonmagnetic substrates have been extensively studied with the interest in quasi-two-dimensional magnetism.[1–5] Most of the researches, however, have been made for ferromagnetic (in their bulk state) thin films on nonmagnetic substrates. The antiferromagnetic (in their bulk state) films have drawn much less attention than the ferromagnetic one, because there has been minor impetus from the application side and partly because it has not been easy to study the antiferromagnetism of the ultrathin films.

Among the few antiferromagnetic (in their bulk state) films, Mn ultrathin film has been one of the most studied systems. The early experimental works were stimulated by the theoretical prediction that the body-centered cubic (bcc) structure of Mn with lattice constant $a_0 \geqslant 2.75$ Å should have a high-spin ferromagnetic ground state.[6] Various experimental efforts have been made to realize bcc Mn phase in the form of thin films, because bcc Mn, δ Mn, exists in their bulk state only between 1406 and 1517 K.

Recent attention has been drawn to the ordered surface alloys of Mn on various substrates, because the magnetic energy associated with the high magnetic moment of Mn dramatically manifests its influence on the determination of their atomic structures. For Mn/Cu(001) system, Mn atoms form $c(2\times2)$ surface confined alloy.[7] The surface confinement, the $c(2\times2)$ order and the pronounced outward buckling of the Mn atoms are driven by the sizable magnetic energy of the Mn atoms.[8] For Mn/Ag(001) system, in contrast, pure Mn monolayer (ML) beneath 1-ML-thick Ag capping layer is more stable than the ordered alloy phases with regards to its energetics.[9] For this system, very low surface free energy of Ag terminated surface plays a dominant role for the stabilization of the subsurface Mn structure. Observed $c(2\times2)$ bilayer alloy is only a kinetically limited, metastable phase near room temperature.[9]

In order to have a systematic picture for the Mn surface alloys on (001) surfaces of the noble metals, we study the growth and the atomic structure of Mn surface alloys on Au(001). Previous works on Mn/Au(001) are very rare. Only a low-energy electron diffraction (LEED) *IV* (spot intensity vs incident electron energy) study for very low coverage of Mn on a Au(001) is found.[10] The main interest of the work is, however, on the effect of Mn impurities on the deconstruction of a reconstructed Au(001), and no structural information of the Mn films is provided. From the present work, we report that there exist diverse structural phases depending on the thickness and the annealing temperature of the Mn films on Au(001), and reveal the atomic structures of two ordered alloy phases by LEED *IV* analysis and discuss the energetic factors stabilizing each alloy phase.

This paper is comprised of five sections. In the following section, experimental procedure is detailed. Then, the results of the LEED *IV* analysis are described. In the Sec. IV, the correlation between the atomic structures of the ordered al-

 ©2002 The American Physical Society

loys and their underlying energetics is discussed.

II. EXPERIMENT

All the experiments are performed in an ultrahigh vacuum chamber with its base pressure in the mid-10^{-11}-Torr range. The chamber is equipped with a cylindrical mirror analyzer Auger electron spectrometer (AES), and a video LEED system[11] as well as standard sample preparation tools.

The Au(001) sample is a top-hat shaped one with its orientational accuracy better than 0.4°. The sample is cleaned by repeated cycles of Ar ion sputtering and subsequent annealing at 700 K for 10 to 30 min. The cleanliness of the sample is checked by AES. The atomic order of the sample is judged by the quality of LEED pattern. For a clean sample, well-defined $p(5\times20)$ reconstructed LEED pattern is obtained.

Mn is deposited by thermal evaporation from a 1-mm-thick Mn chip (99.9%) wound by a tungsten (99.999%) filament. The amount of Mn deposited on a Au(001) is estimated by the intensity ratio of the main AES peaks of Mn and Au, assuming layer-by-layer growth. We call the coverage determined according to this procedure as ''nominal'' Mn thickness, because real growth mode is not known in advance to be layer by layer. All the Mn deposition is made on a Au(001) substrate at room temperature while monitored by a quartz microbalance. Typical evaporation rate is ~ (nominal) 1 ML/5 min. During Mn deposition, the chamber pressure is kept below 5×10^{-10} Torr.

LEED *IV* characteristics for various Mn films on a Au(001) are obtained at room temperature in normal incidence geometry by fully automated video LEED system.[11] Stray magnetic field is reduced below 0.05 Oe by three Helmholz coils perpendicular to each other. The normal incidence geometry is confirmed by the coincidence of the *IV* curves of symmetrically equivalent LEED spots. LEED *IV* curves are obtained from 50 to 400 eV for five symmetrically inequivalent spots, [1,0], [1,1], [2,0], [2,1], [1/2,1/2].

III. RESULTS

Clean Au(001) surface shows a $p(5\times20)$ LEED pattern, which has long been ascribed to the propensity toward the formation of hexagonal close-packed surface layer.[12] The $p(5\times20)$ reconstruction is easily lifted by strongly bound adsorbates such as Mn, Fe, and Rh.[10] We also observe the recovery of the nearly $p(1\times1)$ pattern with nominal 0.1 ~0.2 ML of Mn deposition, though the traces of $p(5\times20)$ pattern are still observed for the electron energies below ~30 eV.

For Mn films with their nominal thickness from 0.3 to 0.4 ML, LEED pattern becomes very poor in its quality and no other spots can be found except (1,0) beam with extremely low intensity. After mild annealing at 500 K for 10 min, however, very sharp $c(2\times2)$ LEED pattern is observed. Our visual inspection tells that the LEED pattern little degrades from that of the clean Au(001) with respect to spot width and the background intensity. We call this ordered surface alloy as SA1.

TABLE I. The observed LEED patterns for Mn/Au(100) system at various thicknesses.

(Nominal) Thickness (ML)	LEED patterns: Room temperature deposition	LEED patterns: After annealing (500 K, 10 min)
clean Au(001)	(5×20)	
~0.2	nearly $p(1\times1)$	(5×20)
0.3~0.4	poor $p(1\times1)$	sharp $c(2\times2)$ (SA1)
0.5~0.8	$c(2\times2)$	poor $c(2\times2)$
0.9~1.5	bright $c(2\times2)$	sharp $c(2\times2)$ (SA2)
1.5~2.5	$p(1\times1)$	$c(2\times2)$

The $c(2\times2)$ LEED pattern develops for nominal 0.5-ML Mn film even without annealing, and persists with increasing Mn thickness up to nominal 1.5 ML. The $c(2\times2)$ superstructure is best defined for (nominal) 1-ML film. After annealing the 1-ML film at 500 K for 10 min, much improved $c(2\times2)$ LEED pattern is obtained, although the LEED spots becomes slightly diffusive and its background intensity is high relatively to that of the clean Au(001). We call this ordered surface alloy, SA2.

For the nominal Mn thickness between 1.5 and 2 ML, relatively sharp $p(1\times1)$ pattern is observed, although a weak trace of the $c(2\times2)$ pattern can still be detected at very low electron energies below 30 eV. For the Mn film from 2.0 ML to 2.5 ML, the $c(2\times2)$ pattern completely disappears, but the $p(1\times1)$ pattern also becomes diffusive. For the Mn films with their thickness between 1.5 and 2.5 ML, the $c(2\times2)$ order still returns after annealing at 500 K for 10 min. They are, however, not so sharp as the SA1 and SA2 phases. Aforementioned Mn phases are summarized in the Table. I.

Before investigating the atomic structures of the two $c(2\times2)$ phases, SA1 and SA2, by LEED *IV* analysis, we make the oxygen titration of surface elements to facilitate the search for the trial structures for fitting the experimental LEED *IV* curves. Mn is very reactive to oxygen, while Au is extremely inert to the oxygen chemisorption at room temperature. Thus, oxygen atom is expected to adsorb selectively to Mn site of the topmost layer, if any Mn atom exists on the surface. Before O_2 dose to the systems in concern, we confirm by AES that oxygen hardly adsorbs at clean Au(001) after 6–10 Langmuir (L) of O_2 dose with oxygen partial pressure, $1-2\times10^{-7}$ Torr. For the SA1, after dosing the same amount of oxygen, the intensity of oxygen main peak is under the detection limit of AES. On the other hand, for the SA2, a distinct oxygen peak is observed in the AES spectra after similar amount of the O_2 dose. From these titration results, we can assume that the topmost layer of the SA1 mainly consists of Au atoms, while a substantial amount of Mn exist at the surface of the SA2.

For the LEED *IV* analysis, the scattering phase shifts of Mn and Au for angular momentum quantum number l up to 8 are employed.[13] Thermal vibration effect is taken into account by Debye-Waller factors with Debye temperatures, 165 K for Au and 410 K for Mn. The LEED *IV* fit is made by the

TABLE II. *R* factor and AES intensity ratio(theory) for various model structure of nominal 0.5-ML coverage.

Structure	*R* factor	AES ratio
Au-Mn/Au(100)	0.5016	0.079
Au-Mn/Au-Mn/Au(100)	0.4835	0.154
Au/Au-Mn/Au(100)	0.2183	0.039
Au/Au-Mn/Au-Mn/Au(100)	0.3765	0.069
Au/Au-Mn/Mn/Au(100)	0.4568	0.077
Mn/Au-Mn/Au(100)	0.5431	0.207
Mn_{50}/Au(100)	0.7337	0.022
Mn_{50}/Au-Mn/Au(100)	0.5809	0.107
Au_{50}/Mn/Au(100)	0.5761	0.087
Au_{50}/Au-Mn/Au(100)	0.4276	0.067
Experimental AES ratio		0.04

automated tensor LEED program.[14] The quality of the fitting is assessed by Pendry reliability (*R*) factor, R_p. The error limit is set by the variance of the Pendry *R* factor.[15]

In the Table II are listed (according to their low *R* factors) selected model structures for the SA1 and corresponding Auger intensity ratio, I(Mn, 592 eV)/I(Au, 74 eV), calculated by employing an empirical formula of Seah[16] for the escape depths of the incident and the Auger electrons. Auger sensitivity factors for Mn and Au are obtained from the database of Physical Electronics Industries Inc.[17] All the models in the Table II comply to the symmetry requirement of the observed $c(2\times2)$ LEED pattern.

The best-fit structure for the SA1 is found to be a $c(2\times2)$ Au-Mn sublayer alloy beneath 1-ML-thick Au capping layer, 1-ML Au/1-ML $c(2\times2)$ Au-Mn/Au(001) with the R_p value of 0.2183. The difference in *R* factor between the best-fit structure and the others is much larger than the variance of *R* factor, 0.04. Experimental LEED *IV* curves and theoretical ones for the optimum structure are compared in the Fig. 1. They show reasonable coincidence in their peak positions

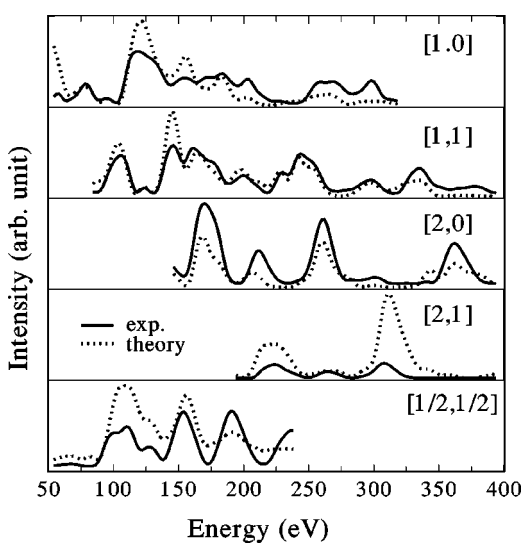

FIG. 1. Experimental (solid line) and theoretical (doted line) LEED *IV* curves for the SA1.

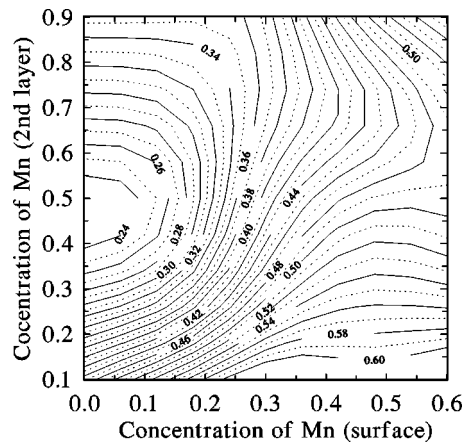

FIG. 2. The contour map of *R* factor as a function of the relative Mn composition(%) of the surface and the second layer for SA1.

and peak intensities. The experimental Auger intensity ratio, $I(\mathrm{Mn},592\ \mathrm{eV})/I(\mathrm{Au},74\ \mathrm{eV})$, is 0.043 in reasonable agreement with the theoretical value, 0.039 for the best-fit structure, taking into account the large uncertainties of the escape depths involved for the calculation of the Auger intensity ratio. The structure is also consistent with the results of the oxygen titration, because the surface layer of the best-fit structure is formed of inert Au atoms. In regards to the proper fitting of the *IV* curve with a low *R* factor, the consistent AES calibration, and the oxygen titration result all combined, we may conclude that the SA1 structure is mainly formed of the Au-Mn sublayer alloy under 1-ML Au layer.

For the possible variation of the chemical compositions from those for the stoichiometrically well-defined model structures, we investigate the chemical composition of each layer by employing average *t*-matrix approximation (ATA).[18] In ATA, each disordered layer is approximated to be homogeneous and composed of pseudoatoms whose scattering *t* matrix is approximated by the composition weighted average of the *t* matrices of Au and Mn. The ATA is successfully applied even to the *ordered* $c(2\times2)$ Mn alloys on Pt(111).[19]

In the Fig. 2 is shown the R_p as a function of relative compositions of Mn in the first two layers of the SA1. There is a well-defined minimum for the Mn concentration of the first layer, $0^{+15\%}_{-0\%}$ and those of the second and the third (not shown in the figure) layers, $50\pm20\%$ and $0^{+30\%}_{-0\%}$, respectively. The minimum *R* factor is slightly lowered to 0.23 by the optimization of the chemical composition in addition to the structural optimization. The optimum atomic structure is changed only slightly from the geometrically optimized one by the inclusion of the compositional optimization. Even though there are uncertainties in the predicted optimum compositions, they still suggest the dominant formation of the Au-Mn sublayer alloy under 1-ML Au capping layer.

The schematics of the best-fit structure for the SA1 is shown in the Fig. 3, and the detailed structural parameters are summarized in the Table III. There is observed relatively small lattice relaxation; The interlayer distances around AuMn alloy layer show contraction by 2.4% and 2.2% in reference to the bulk interlayer spacing of Au(001). The inner layers keep the interlayer spacing of bulk Au(001) with

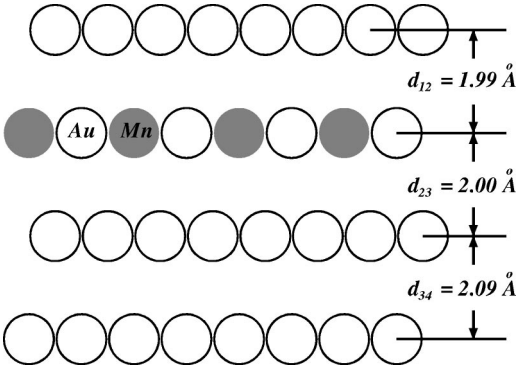

FIG. 3. The best fit structure for the SA1. The filled circles represent Mn atoms and the empty circles do Au atoms. Thick horizontal lines indicate the location of the planes of the ideal bulk terminated Au(001).

minor relaxation. Such a weakly relaxed structure for the SA1 is an unexpected one, because the lattice parameter of the fcc Mn, γ Mn, is smaller by 3.5% than that of Au, and hence the large contraction of the interlayer spacing around the Au-Mn sublayer is expected to compensate the in-plane tensile stress in the alloy layer.

For the SA2 (Table IV), the best-fit structure (ST-I) is a $c(2\times2)$ AuMn/1-ML Mn/$c(2\times2)$ MnAu/Au(001) with the minimum R factor, 0.2396. It is noteworthy that Au atom in the third layer takes the position of Mn in the first layer and vice versa. The structure where the Au (Mn) atom in the third layer takes the equivalent position of Au (Mn) in the first layer (ST-II), $c(2\times2)$ AuMn/1-ML Mn/$c(2\times2)$ AuMn/Au(001), shows the higher R factor, 0.2754. The latter structure should be energetically less favored to the former because the strain builds up normal to the surface by stacking Mn in the first layer on top of the Mn on the third layer. There is found another structure (ST-III), $c(2\times2)$AuMn/1-ML Mn/1-ML Mn/Au(001), with relatively low R factor, 0.2742. The R factors of ST-II and ST-III are, however, marginally within the variance of R factor, 0.056, from the minimum. Hence, the two structures, ST-II and ST-III, are expected to take, if any, only minor portion of the surface.

ST-II and ST-III are different from the best-fit structure (ST-I) only for the third layer. Thus, we examine the chemical composition in the third layer by employing ATA. There are two inequivalent sites, denoted by A and B as in Fig. 7. A (B) is the site where Mn (Au) sits in the first layer. We refine the IV analysis by including the Mn compositions in both sites as additional fitting parameters, and the results are summarized in Fig. 4. Minimum R factor is slightly lowered from that of ST-I, and found at Mn compositions, 0% and 85%, respectively, for A and B sites. It clearly indicates that ST-I dominates the surface.

It may be possible that the three model structures form large domains. Then, the averaged t matrix would vary a lot over the surface, which negates the application of ATA. To deal with such a situation, we also fit the IV by (incoherently) summing the LEED intensities from the three models, while varying the weight of each contribution. R factors as a function of the relative population of ST-I and ST-III is

TABLE III. The best fit structure of the SA1 from LEED IV analysis. $\Delta d_{ij}/d_b$ means the relaxation of the interlayer spacing(d_{ij}) relative to the bulk interlayer spacing(d_b). ΔE is total energy range of inequivalent beams under LEED IV analysis. Pendry reliability factor R_P is employed.

	Interlayer relaxation
$\Delta d_{12}/d_b$	$(-2.4\pm4.8)\%$
$\Delta d_{23}/d_b$	$(-2.2\pm5.2)\%$
$\Delta d_{34}/d_b$	$(+2.4\pm7.9)\%$
ΔE	1242 eV
R_P	0.2183

TABLE IV. R factor and AES intensity ratio(theory) for various model structure (nominal 1 ML).

Structure	R factor	AES ratio
Au-Mn/Au-Mn/Au(100)	0.2916	0.154
Au-Mn/Au-Mn/Au-Mn/Au(100)	0.3447	0.218
Au-Mn/Au-Mn/Mn/Au(100)	0.3122	0.236
Au-Mn/Mn/Mn-Au/Au(100)	0.2396	0.261
Au-Mn/Mn/Au-Mn/Au(100)	0.2754	0.261
Au-Mn/Mn/Mn/Au(100)	0.2742	0.287
Au-Mn/Mn/Au(100)	0.2998	0.176
Mn/Au-Mn/Au(100)	0.3721	0.207
Mn/Au-Mn/Au-Mn/Au(100)	0.4366	0.303
Mn/Au-Mn/Mn/Au(100)	0.4099	0.334
Mn_{50}/Au-Mn/Au-Mn/Au(100)	0.4356	0.186
Mn_{50}/Au-Mn/Mn/Au(100)	0.4865	0.211
Mn_{50}/Mn/Au-Mn/Au(100)	0.3854	0.244
Mn_{50}/Mn/Mn/Au(100)	0.3823	0.280
Au_{50}/Au-Mn/Mn/Au(100)	0.3601	0.144
Au_{50}/Mn/Au-Mn/Au(100)	0.3411	0.167
Au_{50}/Mn/Mn/Au(100)	0.3211	0.192
Experimental AES ratio		0.28

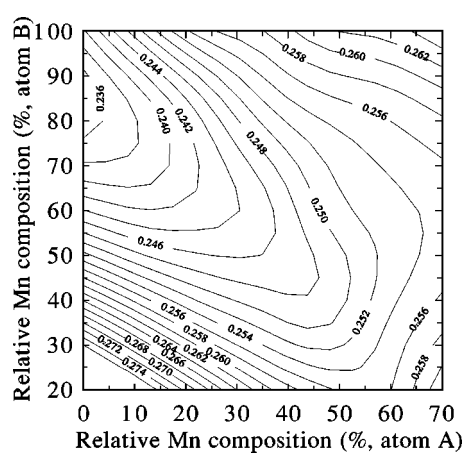

FIG. 4. The contour map of R factor as a function of the Mn compositions in the A nd B sites in the third layer from the surface for the SA2.

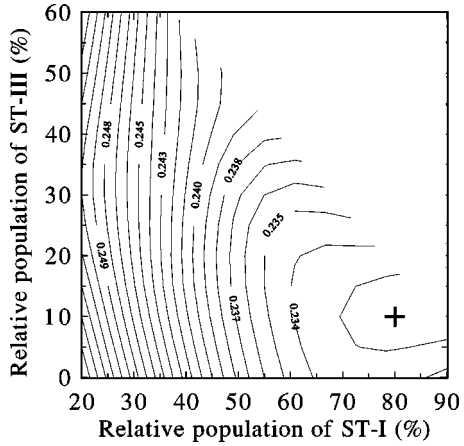

FIG. 5. *R* factor vs relative domain population of ST-I and ST-III. ST-I is $c(2\times2)$ AuMn/1-ML Mn/$c(2\times2)$ Mn-Au/Au(001) and ST-III is $c(2\times2)$ AuMn/1-ML Mn/ 1-ML Mn/Au(001).

shown in Fig. 5. We find the minimum at the relative population of 80, 10, 10% for ST-I, ST-II, and ST-III, respectively. This result reassures that the present system is mainly formed of ST-I, although we cannot definitely tell the relative population.

The experimental Auger intensity ratio, 0.28, for the SA2 is in good agreement with the theoretical value, 0.261 for the best-fit structure, ST-I.[20] ST-I is also consistent with the result of the oxygen titration, i.e., the observation of a considerable amount of the adsorbed oxygen atoms on the surface of the SA2. Hence, all the aformentioned results consistently predict that the SA2 is formed mainly of the ordered surface alloy, $c(2\times2)$AuMn/1-ML Mn/$c(2\times2)$Mn-Au/Au(001), ST-I.

In Fig. 6, the experimental *IV* curves are well reproduced by the theoretical one calculated for ST-I. The best-fit atomic structure is shown in Fig. 7, and detailed information is summarized in Table V. In sharp contrast to the SA1, we find strong atomic corrugation in the surface layer with Mn atoms

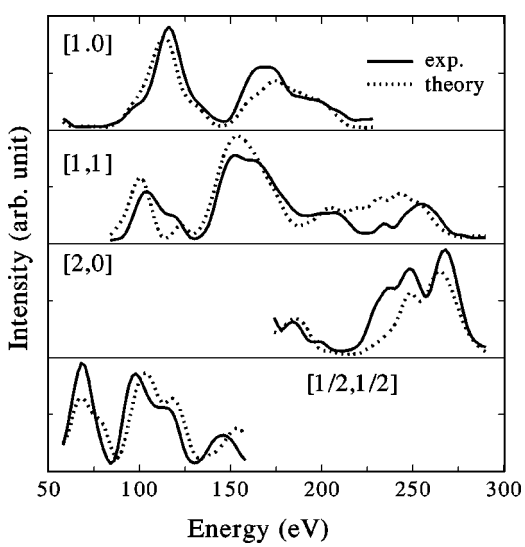

FIG. 6. Experimental (solid line) and theoretical (doted line) Leed *I-V* curves for the SA2.

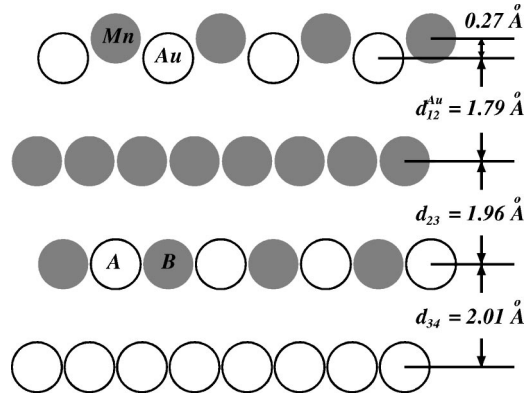

FIG. 7. The best-fit structure for the SA2. The filled circles represent Mn atoms and the empty circles do Au atoms. *A* and *B* indicate the two inequivalent(due to the alloyed surface layer) sites in the third layer from the surface.

buckled up by ~13.4% of bulk interlayer spacing (d_b of Au(001) for the SA2. Besides, all the first three interlayer spacings contract in reference to the d_b of Au(001).

We observe, at least, two different ordered alloy phases for Mn/Au(001) system, the SA1 and SA2 phases(Table I). If we consider the first three layers of the SA1 from the surface, the best-fit structure for the SA1 has the stoichiometry and the atomic structure of the ordered bulk Au_3Mn. The SA2, $c(2\times2)$ Au-Mn/1-ML Mn/$c(2\times2)$ Mn-Au/Au(001), has the stoichiometry of $AuMn_3$ alloy. The diversity of the ordered Mn alloy phases on Au(001) may be attributed to the corresponding bulk alloy phases, because Mn-Au bulk alloy shows very complicated phase diagram with various ordered phases.[21] It is, however, noteworthy that Au_3Mn phase is observed in their bulk phase diagram, while ordered $AuMn_3$ phase is missing. The Mn-richest phase is found only to be $AuMn_2$. Hence, the SA2 is a surface stabilized one.

IV. DISCUSSION

The atomic structure of the surface alloy is determined by the delicate interplay among the energetic factors such as the surface free energy,[22] the strain energy,[23] and now the magnetic energy for Mn alloys[8] as well as the kinetic factors.[24] Sometimes, the low bulk diffusivity makes the surface con-

TABLE V. The best-fit structure of the SA2 from LEED *IV* analysis. $\Delta d_{ij}/d_b$ means the relaxation of the interlayer spacing(d_{ij}) relative to the bulk interlayer spacing (d_b). ΔE is total energy range of inequivalent beams under LEED *IV* analysis. Pendry reliability factor R_P is employed.

	Interlayer relaxation
$\Delta d_{12}^{Mn}/d_b$	$(+1.1\pm2.4)\%$
$\Delta d_{12}^{Au}/d_b$	$(-12.3\pm6.5)\%$
$\Delta d_{23}/d_b$	$(-4.0\pm5.8)\%$
$\Delta d_{34}/d_b$	$(-1.4\pm11.4)\%$
ΔE	652 eV
R_P	0.2396

fined alloy in a local equilibrium among the states accessible with limited bulk diffusion. The SA1 and the SA2 phases look to be the case because the two ordered alloys are stable against prolonged annealing at 500 K. Hence, we may discuss the stability of the SA1 and SA2 according to their energetics.

For the current Mn alloys on Au(001), there is lattice mismatch between γ Mn and Au by $\sim$3.5%, and there should be large strain built in the alloy layers. Mn alloys would relieve the strain more efficiently at the surface than in the bulk, because Mn is less coordinated at the surface. Hence, alloyed layers tend to segregate to the surface. Tersoff[23] found that the surface segregation and the ordering of (nonmagnetic) surface alloys could be explained solely by the strain energy and its relief mechanism. For magnetic alloys such as Au-Mn system, the magnetic energy contributes additionally. The magnetic energy gain is larger when Mn atom is on the surface than below the surface, because the magnetic moment of Mn atom is enhanced with the reduced coordination of Mn on the surface. Thus, the magnetic energy also drives the Mn alloy to segregate to the surface. Such a magnetic contribution is important especially for Mn atom which has half filled *d* shells in its atomic state.[8] Third and contrarily, the small surface free energy of Au terminated surface favors Au atom to be at the surface.

The observed SA1 structure suggests that the surface free energy supercedes the strain and the magnetic energies in the determination of the atomic structure for the SA1 phase. Stepanyuk and Hergert.[25] reported that for all 3*d* atoms deposited on Au(001), the subsurface location of the 3*d* impurity atoms was energetically favored, according to their total-energy calculation employing spin-polarized Korringa-Kohn-Rostoker (KKR) Green-function method. Specifically, the energy difference between the surface and the subsurface locations of a Mn atom was as much as 0.5 eV. Hence, the theoretical result also implies that the low surface free energy of Au terminated surface governs the energetics of both the 3*d* impurities and the SA1, irrespective of the details of each element.

The subsurface residence of the Mn atoms is, however, driven not only by the segregating propensity of the Au atoms to the surface. Mn atoms also favor the subsurface position where it can make more Au-Mn bonds than on the surface, because Au-Mn bond is stronger than Au-Au bond.[25] Similar behavior is also observed for Pd/Cu(110) system, where the surface free energy of the Cu surface layer with a subsurface Pd layer is lower than pure Cu surface layer.[26]

For the Mn atom in the subsurface position, the interaction energy between Mn atoms at the nearest-neighbor sites was reported to be $+0.35$ eV, i.e., there was repulsive interaction.[25] It should not be energetically favorable for two Mn atoms stay next to each other, because, if then, there should be built up large tensile strain. Mn atom also tends to minimize hybridization with other Mn atoms to keep their high magnetic moment and in turn to maximize magnetic energy gain. The formation of the $c(2\times2)$ ordered alloy rather suggests that there is an attractive interaction between Mn atoms at the next nearest neighbor. Tersoff[23] found that strain made (nonmagnetic) impurity atoms at the next-nearest-neighbor sites to feel attractive interaction. From the energetic point of view, the $c(2\times2)$ configuration is also ideal for $Au_{0.5}Mn_{0.5}$ alloy to minimize energetically unfavorable Mn-Mn and Au-Au nearest-neighbor bonds and maximize the favored Au-Mn bond.

For the SA1, we find relatively small relaxation around the Au-Mn alloy sublayer (Table III). If there happened large interlayer contraction to compensate the in-plane tensile strain, however, Mn atom would have reduced magnetic moment and magnetic energy loss due to the increase of the effective coordination number and the concomitant reduction of the magnetic moment of Mn. Observed small relaxation near the surface suggests that the magnetic energy overweighs the strain energy in the determination of the layer spacing of the SA1.

In order to have a microscopic picture for the stability of the SA1, an *ab initio* total-energy calculations based on density-functional theory is carried out, employing the full-potential linearized augmented plane wave method in local spin-density approximation with generalized gradient approximation. We find for the ferromagnetic state of the SA1 that 1-ML Au/1-ML $c(2\times2)$ MnAu/Au(001) is energetically more stable than 1-ML $c(2\times2)$ Mn-Au/Au(001) by relatively big energy difference of $\sim$0.7 eV per unit cell. The formation energy of the subsurface alloy, as defined by 1/2TE[1-ML Au/1-ML Mn/Au(001)]+TE[Au(001)]- TE[1-ML Au/1-ML $c(2\times2)$ MnAu/Au(001)], is calculated to be about 0.13 eV, where TE means total energy. Hence, the alloy formation is favored to the phase-separated state.

For 1-ML Au/1-ML $c(2\times2)$ Mn-Au/Au(001) in both the paramagnetic (PM) and ferromagnetic (FM) states, the total energies are calculated as a function of the interlayer spacings nearby the Mn-Au alloy layer. For the PM state, the interlayer spacings between the surface Au and Mn-Au layers, and between Mn-Au and inner Au layers show larger contraction by 4.6% and 3.2%, than the experimental ones, $\sim$2%. For the FM state, however, the corresponding spacings are calculated to be shrunk only by 0.7% and be expanded by 0.5%, respectively. It confirms that the magnetic energy keeps the interlayer spacing of the SA1 less relaxed from the bulk one.

In sharp contrast to the SA1, the surface of the SA2 is terminated not by Au, but by Au-Mn alloy layer, and there are observed large contraction in the interlayer spacing and the sizable outward buckling of the surface Mn atoms.(Fig. 7, Table V) Aforementioned structural features of the SA2 might be explained in terms of the accumulated strain energy in the trilayer alloy structure and its relief mechanism; As the overall Mn composition is higher and the Mn containing layer is thicker in the SA2 than those of the SA1, the strain energy should play much important role for the stability of the SA2 compared to its role for the SA1. The realization of the SA2 structure tells that the stability gain by the release of the strain energy and the enhancement of the magnetic energy gain overweighs the increase of surface energy in the course of the replacement of the Au surface layer by the Au-Mn alloy layer. For the efficient relief of the strain energy, it is energetically favorable for the Au-Mn alloy plane to take the surface, because the Au substrate is minimally

affected in that configuration by the relaxation of the surface layer for the relief of the internal stress. Such a change of the segregating layer is often found as the thickness of the strained subsurface layer increases. For systems such as Co or Fe/Cu(111), initially Cu atoms segregate to the surface, but, as the film gets thicker, Co or Fe takes the surface to reduce the strain energy by minimizing its contact with the substrate.[27]

According to above picture, one of the reason for the absence of the SA2-like *bulk* alloy may be that there is no such an efficient mechanism as the surface relaxation for the bulk alloy to relieve the large strain energy built by the high Mn composition, and thus the solubility of the ordered Mn in bulk Au is limited by the strain energy induced by Mn solute. In fact, the maximum solubility of the ordered Mn in Au is 67% for the $AuMn_2$ alloy.[21]

V. SUMMARY AND CONCLUSION

We study the growth of Mn ultrathin films on Au(001) and find two well-defined ordered surface alloys. The atomic structures of those alloys are studied by LEED *IV* analysis. The first alloy contains a sublayer $c(2\times2)$ Au-Mn layer beneath 1-ML-thick Au capping layer, 1-ML Au/ 1-ML $c(2\times2)$Au-Mn/Au(001). This structure is dictated by the distinctly low surface free energy of Au compared to that of Mn. There is little surface relaxation, which, we find from *ab initio* spin-polarized total-energy calculation, results from the magnetic pressure of Mn atoms. The second surface alloy is formed mainly of 1-ML $c(2\times2)$ Au-Mn/1-ML Mn/1-ML $c(2\times2)$ Mn-Au/Au(001), where the positions of Au and Mn in the first layer are exchanged in the third layer. We find the large contraction for the three interlayer spacings from the surface, compared with the interlayer spacing of the bulk Au(001), d_b(Au(001)), and also the strong outward buckling of the Mn atoms in the surface layer by $\sim$13.4% of d_b(Au(001)). Contrary to the SA1, the structure of the SA2 is determined mainly by the strain energy of the Mn containing layers due to the higher Mn composition and the thicker Mn containing layers than those of the SA1.

ACKNOWLEDGMENTS

J.-S.K. appreciates M. Wuttig for helpful comments. This work was supported by MOST [KISTEP 00-B-WB-07-A-01(J.-S.K.) and Nano-Technology Project ('00)(S.-J.O.)], by KOSEF [ASSRC (S.C.H.)] and by Korea Research Foundation (KRF-99-0005-E00018)(H.G.M.).

*Present address: Center for Atomic Control of Heteroepitaxy (CACH), Korea Research Institute for Standards and Science, 130-743, Korea.

[1] F.J.A. den Broeder, W. Hoving, and P.J.H. Bloemen, J. Magn. Magn. Mater. **93**, 562 (1991).
[2] S. Blügel, M. Weinert, and P.H. Dederichs, Phys. Rev. Lett. **60**, 1077 (1988).
[3] C. Hwang, A.K. Swan, and S.C. Hong, Phys. Rev. B **60**, 14 429 (1999), and references therein.
[4] B. Heinrich and J.A.C. Bland, Eds., *Ultrathin magnetic Structures* (Springer Verlag, Berlin, 1994).
[5] G.A. Prinz, J. Magn. Magn. Mater. **200**, 57 (1999).
[6] V.L. Moruzzi, Phys. Rev. Lett. **57**, 2211 (1986); V.L. Moruzzi, P.M. Marcus, and P.C. Pattnaik, Phys. Rev. B **37**, 8003 (1988); V.L. Moruzzi and P.M. Marcus, *ibid.* **38**, 1613 (1988).
[7] M. Wuttig, Y. Gauthier, and S. Blügel, Phys. Rev. Lett. **70**, 3619 (1993).
[8] S. Blügel, Appl. Phys. A: Mater. Sci. Process. **63**, 595 (1996).
[9] W. Kim, W. Kim, S.-J. Oh, J. Seo, J.-S. Kim, H.G. Min, and S.C. Hong, Phys. Rev. B **57**, 8823 (1998).
[10] S.C. Wu, H. Li, J. Quinn, D. Tian, Y.S. Li, A.M. Begley, S.K. Kim, F. Jona, and P.M. Marcus, Phys. Rev. B **49**, 8353 (1994).
[11] S.H. Kim, K.S. Lee, H.G. Min, J. Seo, S.C. Hong, T.H. Rho, and J.-S. Kim, Phys. Rev. B **55**, 7904 (1997).
[12] D.G. Fedak and N.A. Gjostein, Phys. Rev. Lett. **16**, 171 (1966); S.G.J. Mochrie, D.M. Zehner, B.M. Ocko, and D. Gibbs, *ibid.* **64**, 2925 (1990).
[13] V.L. Moruzzi, J.F. Janak, and A.R. Williams, *Calculations of Electronic Properties of Metals* (Pergamon, New York, 1978).
[14] P.J. Rous, J.B. Pendry, D.K. Saldin, K. Heinz, K. Müller, and N. Bickel, Phys. Rev. Lett. **57**, 2951 (1986); P.J. Rous, Prog. Surf. Sci. **39**, 3 (1992).
[15] J.B. Pendry, J. Phys. C **13**, 937 (1980).
[16] S. Mroz, Prog. Surf. Sci. **46**, 377 (1994).
[17] L.E. Davis, N.C. MacDonald, P.W. Palmberg, G.E. Riach, and R.E. Weber, *Handbook of Auger Electron Spectroscopy*, 2nd ed. (Perkin Elmer Corporation, Eden Prairie, 1976).
[18] F. Jona, K.O. Legg, H.D. Shih, D.W. Jepson, and P.M. Marcus, Phys. Rev. Lett. **40**, 1466 (1978); Y. Gauthier and R. Baudong, in *Surface Segregation Phenomena*, edited by P.A. Dowben and A. Miller (CRC, Boca Raton,1990).
[19] S. Gallego, C. Ocal, M.C. Munoz, and F. Soria, Phys. Rev. B **56**, 12 139 (1997).
[20] We do not attempt to determine the relative population of each structure from the Auger intensity ratio because of the large uncertainty of the theoretical Auger intensity ratio originating from the wide variation of the reported escape depths.
[21] *Phase Diagrams of Binary Gold Alloys*, edited by H. Okamoto and T.B. Massalski (ASM International, Metals Park, 1987).
[22] H. Röder, R. Schuster, H. Brune, and K. Kern, Phys. Rev. Lett. **71**, 2086 (1993).
[23] J. Tersoff, Phys. Rev. Lett. **74**, 434 (1995).
[24] F. Besenbacher, L.P. Nielsen, and P.T. Sprunger, in *The Chemical Physics of Solid Surface*, edited by by D.A. King and D.P. Woodruff (Elsevier Science, Amsterdam, 1997), Vol. 8, p. 207.
[25] V.S. Stepanyuk and W. Hergert, Phys. Rev. B **62**, 7542 (2000).
[26] P.W. Murray, S. Thorshaug, I. Stensgaard, F. Besenbacher, E. Laegsgaard, A.V. Ruban, K.W. Jacobsen, G. Kopidakis, and H.L. Skriver, Phys. Rev. B **55**, 1380 (1997).
[27] A. Christensen, A.V. Ruban, P. Stoltze, K.W. Jakobsen, H.L. Skriver, J.K. Nørskov, and F. Besenbacher, Phys. Rev. B **56**, 5822 (1997).